

Yaliang Gui¹, Mario Miscuglio¹, Rubab Amin¹, Hao Wang¹, Jacob K. Khurgin², Hamed Dalir^{1,a}, and Volker J. Sorger¹

100 GHz Micrometer-compact broadband Monolithic ITO Mach–Zehnder Interferometer Modulator enabling 5000 times higher Packing Density

¹Department of Electrical and Computer Engineering, George Washington University, Washington, DC 20052, USA

²Department of Electrical and Computer Engineering, Johns Hopkins University, Baltimore, Maryland 21218, USA

^aAuthor to whom correspondence should be addressed: hdalir@gwu.edu

Abstract: Electrically programmable application-specific integrated circuit for machine learning and signal processing use electro-optic modulators. However, both foundry-ready silicon and Lithium-niobate-based modulators fall short of high chip packing density and quicker speed. Due to efficient light-matter interactions, current-driven Indium tin oxide (ITO)-based modulators can do both. We demonstrate micrometre-scale Mach-Zehnder interferometer (MZI)-based modulators with switching speeds exceeding 100 GHz. A tiny MZI phase shifter with $V_{\pi}L=0.1\text{V}\cdot\text{mm}$ may be built using ITO-thin sheets over a photonic waveguide. This allows for the integration of over 5000 of these modulators into the same chip area as a single silicon MZI modulator. The modulator design discussed here uses an asymmetric MZI tuning step to optimize the extinction ratio-to-loss ratio. This device is the first to handle next-generation modulator needs for machine intelligence revolution processors, edge and cloud computing, and optical transceivers.

Keywords: electro-optic modulators, programmable ASIC, transparent conductive oxides, Mach-Zehnder interferometer

1 Introduction

Electro-optic modulators (EOMs) [1,2] which switch optical signals based on electrical data streams, are essential components of photonic integrated systems, dictating achievable transmission rate, energy consumption, and chip-integrability of next-generation telecommunication systems and computing hardware. With looming technological advances such as the internet-of-things [3], network-edge computing [4, 5], neuromorphic computing [6, 7], chip-scale light detection and ranging (LiDAR) [8]; the need for increasingly efficient and miniaturized EOMs is relentless. Current

foundry MZI-based modulators (MZM), while being reasonably fast (~ 40 GHz), require a large footprint on the order of 1 mm^2 [AIM, AMF...]. Using an electronic processor die as a footprint-guide ($1\text{ cm}^2 = 100\text{ mm}^2$), the number of PIC components on-chip is severely limited to about 100-1000 components as compared to electronic counterparts. In the photonics community, we argue that photonic-processors scale differently than electronics; this is true given by a) multiplexing options and b) synergistic complexity scaling reductions to algorithms. To share one such example for an algorithm-to-hardware mapping, we can look at performing complex convolutions optically as much simpler dot-product multiplications in the Fourier domain. While this is known in signal processing, the required overhead-heavy Fourier transportation (FT) is performed effortlessly (passively) by an optical lens (either in free space or on a PIC). Mathematical operations scale with a nominal dimensionality factor N , reflecting the runtime complexity (under brute-force, that is, meaning without parallelization strategies). Tensor operations and convolutions, for example scale with N^3 and N^4 , respectively, assuming a squared matrix of size N . Why is this relevant for modulators? Because the performance (typically stated in throughput per second per power, i.e., $\text{TOPS/W}=\text{TOP/J}$) of an accelerator is a direct function of the speed of each modulator and the number of modulators on the ASIC PIC. Hence, being fast and compact becomes critically important for next-generation photonic ASICs (ASPIC).

To address these relevant information processing trends using reconfigurable photonic circuits and hence modulators, several EOM devices schemes have been proposed to enhance Si-based devices' performance only to reveal inadequate improvements beyond the basic and selectively doped junctions [9]. In this view, alternative electro-optic materials for active modulation are sought, offering higher index tunability, seamless integration on the Si platform, ease of relevant processing, and fast modulation in a compact form factor. A plethora of materials have been investigated for this purpose in recent years ranging from the traditional III-V materials [10], polymers [11], ferroelectric materials [12] to more exotic 2-dimensional materials, including graphene [13], transition metal dichalcogenides [14], etc. In this regard, a class of materials that have received growing interest is

transparent conducting oxides (TCOs). TCOs usually feature a fairly wide-bandgap with degenerate doping levels to facilitate electrical conduction while remaining transparent in the widely utilized telecom C-band.

Indium tin oxide (ITO) is the most widely used TCO material in industry and research alike; it offers current-based modulation in an electrical capacitive arrangement based on similar carrier dispersion dynamics as Si. Compared to other materials, integrating ITO in chip-scale modulation schemes presents the following advantages: (i) Availability of at least 3-4 orders of magnitude higher carrier density compared to Silicon; (ii) Dramatic effect of change in carrier concentration on its optical index, which arises from the small permittivity of the material, i.e., $\partial n = \partial \epsilon^{1/2} \sim \partial \epsilon / 2\epsilon^{1/2}$; (iii) The presence of an epsilon-near-zero (ENZ) region in the tolerable carrier concentration range within the electrostatic gating constraints; and (iv) Potential CMOS compatibility, which renders it integrable in the mature Si process flow in a monolithic manner [7], [15]–[17]. The latter is a critical factor, enabling mass scale integration and moving the modulators out of the lab into technology development and production.

Pioneering works in ITO-based absorption modulation influenced interest in its efficacy as a phase modulator stemming from the well-known Kramers-Kronig (K-K) relations [18]. Recently, we identified that phase tuning efficacy surpasses that of absorption tuning for ITO in associated performance metrics [19]. Indeed, ITO is an exciting alternative for highly performing phase modulation as such has been manifested by our recent works supporting half-wave voltage and active device length products, $V_\pi L$ down to 63 V· μm for a lateral configuration device [20]. We have also recently demonstrated noteworthy results in terms of $V_\pi L$ in traditional photonic and plasmonic designs obtaining 520 V· μm and 95 V· μm , respectively [17, 21, 22]. A comparison of disparate performance metrics for different material and model-based schemes found in recent literature is presented for reference (Table 1). Different phase modulation schemes have been investigated with ITO thus far to include traveling wave-based solutions as well as cavity-based approaches [15–25]. In our comparison, cavity-based approaches are not considered since microring resonators can offer a higher extinction ratio (ER) with a slight change in the index but come at the cost of significantly reducing the spectral bandwidth owing to the finesse of the cavity. Additionally, the feedback schemes (e.g., ring circumference or photonic crystal mirror sections) cannot be excluded from the footprint calculations of the active device as these specify the needed finesse of the cavity, which is integral to the device performance of said devices integrated within them. On the other hand, traveling wave-based schemes such as MZIs are single-pass arrangements that can deliver the full broadband optical response the chosen optical mode offers depending on the arms' imbalance. Furthermore, the entire MZI area can be reduced to only the active device footprint plus the spacing for another MZI arm and Y-couplers without any conceivable effect to hinder the

device's performance. This can, de facto, be achieved in a minuscule footprint owing to lithographic advancement in recent years paired with cutting-edge fabrication facilities. Recapitulating the efforts to minimize the real estate on the chip, plasmonics can serve as a reasonable alternative approach to traditional photonic packaging. Plasmonics effectively squeezes the light in the optical mode to enhance light-matter interaction (LMI) with the active modulation material realizing ultrashort devices with improved modulation metrics. Such enhancements in active performance do inherently accompany additional loss in the form of insertion loss (IL) due to the high modal mismatch when coupling back and forth from the underlying Si waveguide. These losses can be partially mitigated by employing modal transitional architecture within the coupling regions in the vicinity of the active device, for example, tapered waveguide sections for plasmonic slot designs. We have shown that the enhanced LMI alleviates the high loss per unit length encountered in plasmonics, and the performance benefits outweigh the initial surcharge of IL if the latter is managed to retain at a tolerable limit [19, 25]. The high real index tuning in ITO accompanies a considerable modulating loss directly resulting from the imaginary part of the index via K-K relations, and this effect is even stronger in the plasmonic mode-based setups as the confinement can reach at least one order of magnitude more than the photonic case. Simple integration of an ITO-based modulator in one arm of an MZI thus limits attainable extinction and refrains from a linear operation, inducing substantial chirp accrual in the process. We have mitigated this issue by imposing some static loss in the form of a passive metallic contact on the other unmodulated arm of the MZI in our previous works with a view to minimizing the loss imbalance in both arms [17, 21, 22]. The static passive metallic method balances the output by introducing loss on the passive arm, increasing insertion loss. One alternative approach is to design the input Y-junction to deliver more power to the active arm to minimize the imbalance resulting upon active switching, decrease IL, and reduce the number of required fabrication steps.

What's more, this asymmetric Y-junction design can also be used to achieve low IL by delivering less power to the active arm. Whether to provide more power to the active arm to minimize the imbalance or deliver less power to increase the imbalance but decrease the IL depends on the applications.

In this work, we introduce an ITO-plasmon-based asymmetric MZI modulator working under low bias conditions and discuss considerations involving device design, such as device length, dielectric thickness, and splitting ratio, for instance; aimed at achievable performance metrics including tolerable IL, adequate ER, low electrical resistance leading to multi-GHz operational speeds, etc. Our design strategy, which can be applied to other material frameworks, enables unitary ER/IL without sacrificing footprint (<5 μm phase shifter, and 2·10⁻⁴ mm²). Additionally, the crafted material properties and appropriately tuned thicknesses lead to superior

electrostatic performance, aiding unprecedented switching speed (up to 100 GHz) and one order of magnitude lower low energy consumption (180 fJ/bit) with respect to state of the art (Table 1). Such performance heralds a new device makes it a strong candidate to become the

Table 1: Figure of merit comparison for different type Mach-Zehnder interferometric modulators.

Material	Mechanism	Length (μm)	ER (dB)	IL (dB)	Speed (GHz)	$V_{\pi}L$ ($V \cdot \mu\text{m}$)	Energy consumption (fJ/bit)	Ref.
LN	Pockels effect	20000	30	0.4	45	2800	0.37	[27]
Si	plasma dispersion effect	15000	3.8	10	10	3300	138000	[28]
Polymer	Pockels effect	1000	10	6	12.5	500	0.7	[29]
ITO	plasma dispersion effect	1.4	8	6.7	1.1	95	2100	[16], [21]
ITO	plasma dispersion effect	4.7	3*	2.9*	100*	108	380*	This Work

Note numbers with '*' its calculated value.

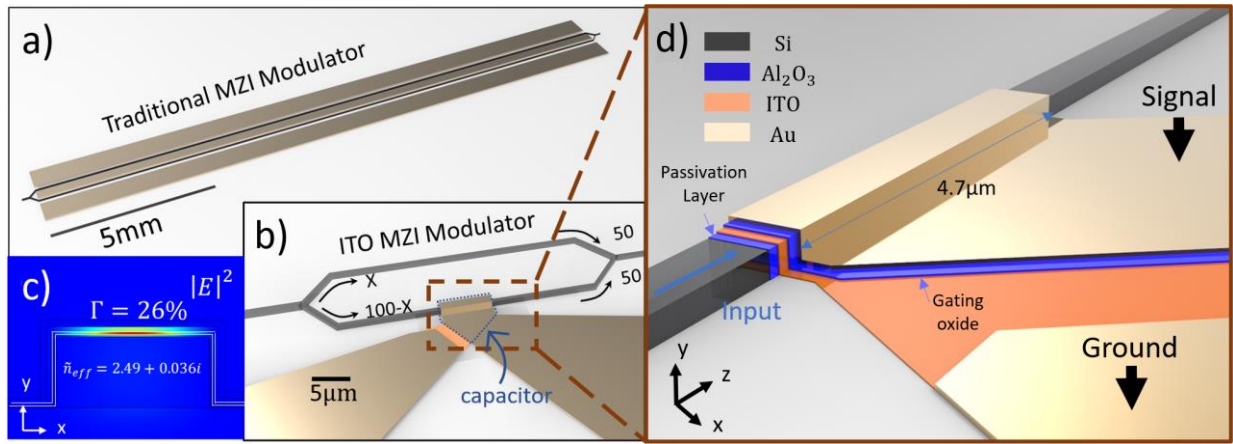


Fig. 1: ITO-based plasmonic MZI modulator on Si photonic platform. (a) Footprint comparison between ITO MZI modulator and traditional MZI modulator. The ITO-based plasmonic MZI modulator with input and output grating couplers is 1mm long and $165\mu\text{m}$ in width, including the contact pads. The size of ITO-based plasmonic MZI is $33\mu\text{m}$ in length and $6\mu\text{m}$ in width. The distance between the grating coupler and the device is longer than $500\mu\text{m}$ to facilitate measurement. (b) Perspective view of the Mach-Zehnder structure with the active biasing contacts. The power splitting ratio for the active arm is X, and the splitting ratio for the passive arm is 100-X. (c) Electric field distribution by performing FEM at 1550nm under +3.5V in the cross-sectional structure for a z cutline along the central region of the Si waveguide (width: 500nm ; height: 220nm). (d) Composition layers of ITO MZI modulator. ($T_{\text{passivation}} = 5\text{nm}$; $T_{\text{ITO}} = 10\text{nm}$; $T_{\text{gating}} = 15\text{nm}$; $T_{\text{Au}} = 30\text{nm}$)

2 Results and discussion

We aimed to design a high-performance electro-optic modulator based on ITO following the high-level rationale outlined above. We carefully analyzed material properties and the design of the modulator to reach an optimized point in terms of tradeoffs between ER and IL within the constraints of small phase shifts. Modulators are inherently optimization-sensitive devices. There is no single best design as many parameters are cross- and inter-dependent (Fig. 2a). As such, we bound ourselves by a set of performance requirements. While these are arbitrarily chosen, they are informed by the rationale above for next-generation modulators with a option for ASPICs and defined as follows: $\text{ER} > 3 \text{ dB}$, $\text{IL} < 3 \text{ dB}$, (i.e. $\text{ER/IL} >$

fundamental building block of the next-generation photonic platform with immediate applications in neuromorphic computing [25] and programmable photonic circuits [26].

1), $\text{f3dB} > 100\text{GHz}$, footprint $> 10\text{-}3 \text{ mm}^2$, and energy consumption $\sim 100 \text{ fJ/bit}$. More design performances are shown in Fig.4f. Secondly, we discuss the above-introduced asymmetric splitting ratio of the front-end Y-junction of the MZI as a secondary application wised optimization strategy, based on the following rationale; the loss induced by the active arm of the modulator (phase shifter) is accounted for by an upstream Y-junction, characterized by an uneven splitting ratio (e.g., 41:59, Fig. 1b), as a function of insertion loss, and modulation depth. A 5 nm thin film of Al_2O_3 is placed on top of the SOI MZI as a passivation layer, enhancing the grating coupler's coupling efficiency. The ultra-thin Al_2O_3 film is chosen based on the fabrication techniques and to maximize the confinement factor. Light modulation is achieved by phase-shifting the mode in one arm of the MZI modulator via electrostatically tuning the free carriers of a 10 nm ITO layer in a parallel plate capacitor configuration.

Additionally, the metal layer used as the top plate of the capacitor generates a plasmonic mode, enhancing light-matter interaction and obtaining strong, effective modal index variation upon carrier concentration tuning in the

ITO film (Fig. 1c). As further discussed, the gating oxide thickness is selected to compromise speed performance and avoid metal ohmic losses.

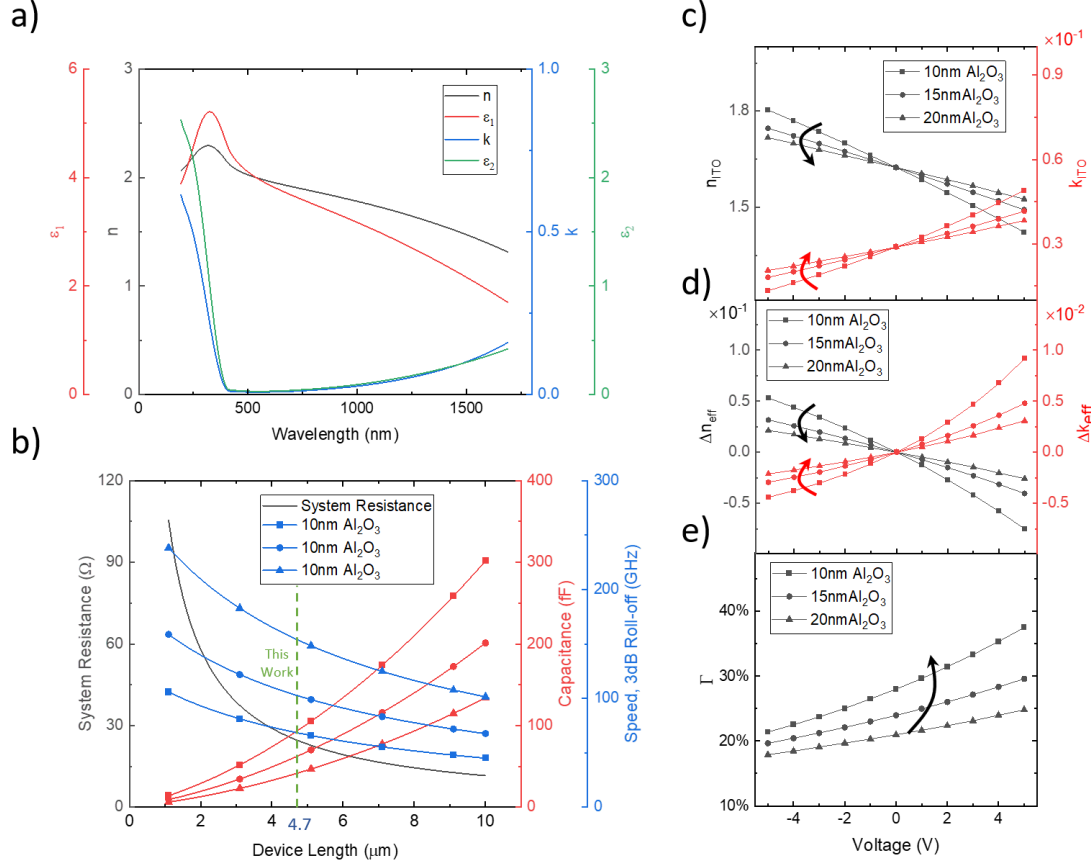


Fig. 2: Tailored material and design parameters of the Phase shifter. a) Dispersive spectrum of 10nm ITO thin film measured by ellipsometry b) Resistance and speed of ITO MZI modulator with a gating oxide thickness of 10nm, 15nm, and 20nm. c) Refractive indices and extinction coefficients of 10nm ITO thin film for various dielectric thicknesses under different voltages. d) Effective mode index differences change with dielectric thickness under varied voltages. e) Confinement factor Γ varies with dielectric thickness and voltages.

The modulation mechanism in ITO is free-carrier dispersion-based accumulation/depletion (Fig.2a). The carrier concentration of unbiased ITO thin film is experimentally measured and reported as $2.07 \times 10^{20} \text{cm}^{-3}$ [16]. The electrical properties of the phase shifter device are calculated from ITO resistivity of $2.9 \times 10^{-4} \Omega \cdot \text{cm}$ after thermal annealing (Fig.2b) [30]. The ITO optical properties are opportunistically tailored tuning deposition techniques to concurrently limit off-state optical losses and keep on-state away from epsilon-near-zero higher losses. This is important since an MZI should be more sensitive

with respect to phase than with amplitude modulation [31,32]. Free carriers can be depleted or accumulated in the active ITO region upon capacitive operation under the bias. From the Drude model, with electrons accumulated or depleted between the dielectric and ITO interface, a

blue- or red-shift of the plasma frequency can be expected by applying a positive or negative voltage, respectively. Strictly speaking, the real part of the refractive index of the ITO thin film decreases for increasing positive voltages corresponding to a blue shift in wavelength. In contrast, the imaginary part increases towards a more metallic characteristic (Fig.2c). Assuming a fixed, CMOS compatible voltage of $\pm 3.5\text{V}$, carrier dynamic charge accumulation ΔQ is inversely proportional to the dielectric thickness. ($\Delta Q = C \times \Delta V$, and $C = \epsilon_0 \epsilon_r A / d$, where $\Delta Q, C, \Delta V, \epsilon_r, A, d$ denoting the accumulated charge, capacitance, changed voltage, the relative dielectric constant, area of two overlap plates, dielectric thickness). In other words, under the same voltage bias, a thinner dielectric can influence a large refractive index and extinction coefficient variation.

To optimize the modulation performance of the proposed phase shifter, compensate for losses, and tune the design parameters, we study the effective mode index variation by performing eigenmode simulation using FEM analysis. The variation of the effective refractive Δn_{eff} is a monotonically decreasing function of the applied voltage (Fig.2d).

The slopes of the curves are governed by the oxide thickness, which is responsible for modulation depth per unit length and loss per unit length. With a superlinear proportionality, the electric field distribution is associated with the propagating mode, thus altering the overlap factor with the active layer (Fig.2e). A thinner dielectric layer leads to a stronger confinement factor, therefore, stronger carrier interaction and a higher ER. However, it also induces higher loss, according to Kramers-Kronig

relations. Under the accumulation state, Δn_{eff} of device with 10nm gating oxide is two times larger than that of device with 15nm gating oxide because of stronger light-matter interaction. Once the phase shift (Δn_{eff}) and related absorption coefficient is obtained, we can define the phase shifter footprint according to the desired modulation depth and derive the modulation speed as a function of the oxide thickness.

Footprint has a strong impact on RC delay (Fig. 2b). Even if a larger overlap area of the two plates would considerably reduce the voltage to be applied or eventually improve modulation depth providing π -shift for the same voltage applied, it would significantly compromise device speed. In contrast, thinner oxide which can improve speed performance (lowering capacitance) would reduce tradeoffs in terms of optical losses.

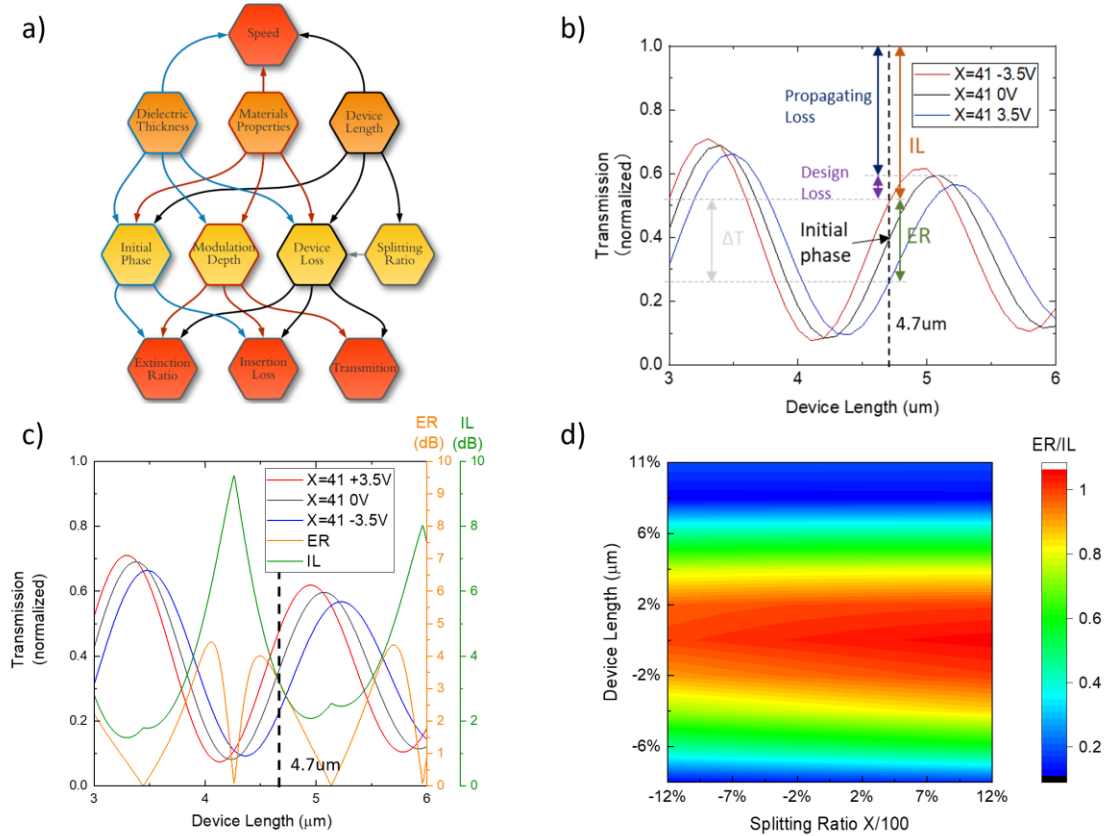


Fig. 3: a) Flow chart of Mach-Zehnder modulator analysis. Variables are dielectric thickness (gating oxide thickness), material properties, device length, and splitting ratio. The performances are ER, IL, transmission, and speed. b) Transmission of ON state, 0 bias state, and OFF state oscillate within the device with a dielectric thickness of 15nm under voltage of +3.5V, 0V, and -3.5V when splitting ratio is 41:59. Propagating loss is caused by absorption, while the design loss is caused by insufficient phase shift. c) Transmission, corresponding ER, and IL varies with device length. ER=3dB and IL =2.9dB when device length is 4.7μm. d) Fabrication tolerance of device length and splitting ratio for the proposed device.

Here we distinguish amongst, propagating loss, defined by $\alpha = \frac{4\pi k_{eff}}{\lambda} = 0.27 \text{ dB}/\mu\text{m}$ and design loss, caused by insufficient modulation depth (phase shift of 0.33π). Ideally, for a complete π shift device, design loss would be 0. The initial phase is dependent on the device length and

the difference between effective mode indexes of two arms. (Fig.3b) In this work, we opted for a total phase shift of 0.33π ($\Delta n_{eff} = 0.1516$), corresponding to 3dB modulation depth and total insertion loss (sum of

propagating loss and design loss) of 2.9 dB for an active region of just $4.7\mu\text{m}$ (Fig.3c).

Additionally, we verified the impact of fabrication tolerances on the phase shifter performance; with a $\pm 4\%$ tolerance in device footprint and over $\pm 12\%$ tolerance in splitting ratio (splitting ratio of $\pm 8\%$ is the current foundry tolerance), we can still achieve an ER/IL=0.8, demonstrating reasonably achievable robustness, certainly given foundry precision. (Fig.3d) To be noticed, the robustness is at the expense of unity decreasing or

increasing of the ER and IL. The details about the ER and IL will be discussed in the following context.

Considering the aforementioned constraints, we select a 15nm gating oxide which allows altering the ITO carrier concentration from $1.6 \times 10^{20}\text{cm}^{-3}$ to $2.5 \times 10^{20}\text{cm}^{-3}$ under $\pm 3.5\text{V}$ electrostatic gating while still ensuring fast modulation (up to 100 GHz) and optimized losses against modulation (ER/IL=3/2.9=1.03). The -3dB roll-off is estimated through RC delay, given the capacitance of 62 fF (blue dash line in Fig 1b) and the total resistance of $25\ \Omega$, while dynamic switching energy is 380pJ.

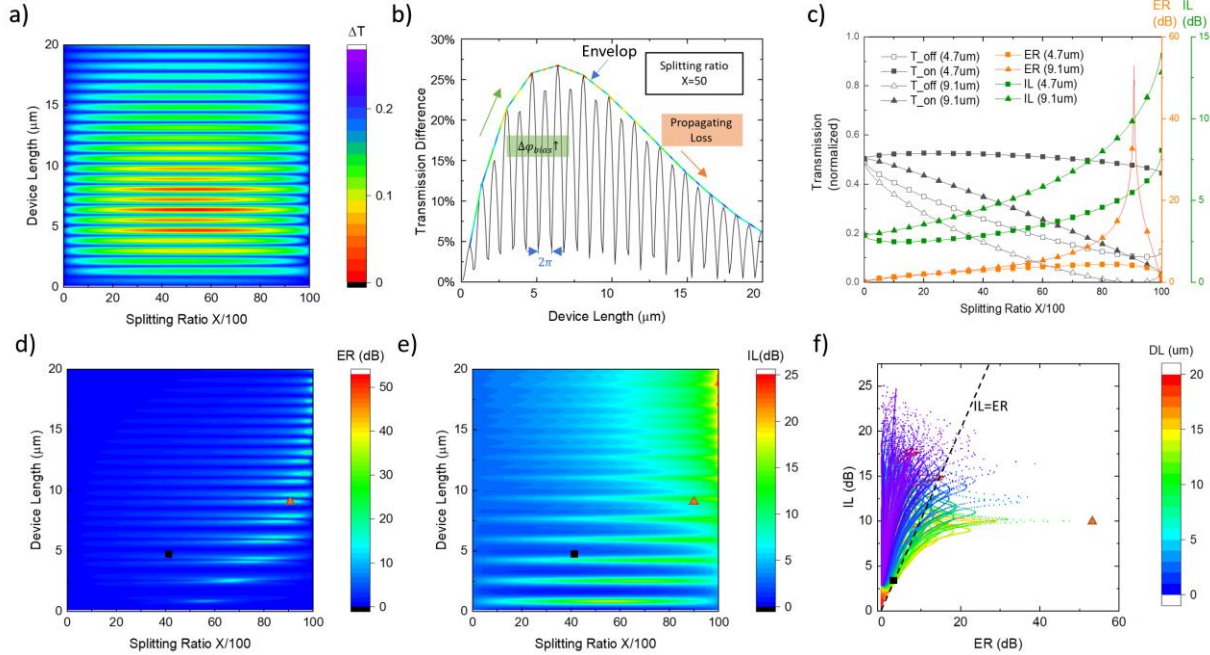


Fig. 4: The performance map of asymmetric plasmonic mode ITO-based MZI modulator with 15nm Al_2O_3 under ON (-3.5V) and OFF states (+3.5V). Squares represent the device with 3dB ER, 2.9dB IL, 25% ΔT , and a speed of 102GHz. Triangle represents the device with 53dB ER, 10dB IL, 10% ΔT , and speed of 71GHz. a) Transmission difference varies with splitting ratio X and device length $0\ \mu\text{m}$ to $20\mu\text{m}$ (More details for photonic mode device is included in SI) Plasmonic designs with transmission differences higher than 25% locate around $5\mu\text{m}$ because of high propagating loss of the longer device. b) Transmission difference of plasmonic mode varies with device length at splitting ratio 50:50. The transmission oscillates because of phase shift by both device length and bias. And the colorful envelope is manually added to show the transmission difference changes with the phase shift caused by the bias and propagating loss. c) Examples: transmissions under ON and OFF state, ER, and IL for devices with lengths of $4.7\mu\text{m}$ ($X=41$) and $9.1\mu\text{m}$ ($X=91$) respectively. d) Extinction ratio of plasmonic mode and photonic device varies with splitting ratio for different lengths. e) Insertion loss of plasmonic mode and photonic mode varies with splitting ratio for different lengths. f) Performance map for device length ranging from $0.1\mu\text{m}$ to $20\mu\text{m}$.

The performance map can be used to find the design with the desired performance (in this work, we randomly pick $\text{ER} > 3\ \text{dB}$ and $\text{IL} < 3\ \text{dB}$). Here, transmission difference is discussed with ER and IL since it's straightforward and facilitates the analysis. The transmission difference of plasmonic mode oscillates with the device length because of periodical initial phase change caused by the varied device length. (Fig. 4a). The envelope of the transmission difference with a splitting ratio of 50:50 in Fig.4b is dominated by the modulation depth and propagating loss. Both of them increase with device length. So, the envelope is device length dependent. It rises in the short length region because modulation depth increases with the device length and mainly affects the shape of the envelope. Then it

decreases in the long length region because the loss of the device on the active arm increases with device length faster than the modulation depth and changes the shape of the envelope. If the propagating loss of the device on the active arm is negligible, ER reaches the largest value with a splitting ratio of 50:50 and a specific initial phase. The initial phase can be obtained by using particular device lengths or asymmetric MZI arms. However, the propagating loss of the plasmonic mode device on the active arm is not negligible. And a high splitting ratio $X > 50$ compensates for the propagating loss but also increases the total loss and reduces the output transmission. The sweet spot is usually below the splitting ratio that gives the maximal ER. The maximum ER represented by using the triangle symbol in

Fig.4c is 53 dB which is achieved by the splitting ratio of 91:9. The amplitude difference of passthrough light from two arms is below 10^{-5} when the device is operating in an OFF state (destructive interference). However, compared with the device we proposed (3dB ER, 2.9dB IL, and 25% ΔT), the device with 53dB ER has a longer length of 9.1 μ m, lower speed of 71GHz, higher IL of 10dB, and lower ΔT of 10%. High ER can be achieved by compensating the device loss (including propagating loss and design loss) using a high splitting ratio ($X > 50$) (Fig.4d). And the splitting ratio of maximum ER design increase with device length because of increasing device loss. IL changed periodically with device length because initial phase changes and varied with splitting ratio because of increasing device loss. (Fig.4e)

For applications with limited phase shift but requires high ER, high IL is expected as a tradeoff. (SI). The same concept also applies to the minimal IL device design. Based on the desired performance requirement and the nonnegligible propagating loss of the device, a low splitting ratio of 41:59 is used for the design. The modulation depth is reduced, but transmitted power is enhanced. This design perfectly balances the tradeoff between the ER and IL and meets the requirements. The ER&IL map in Fig. 4f shows more design options.

3 Conclusion

Within the limits of minor phase shifts, we investigated material qualities as well as the design of the modulator to arrive at an optimal position in terms of tradeoffs between ER and IL. The results of this investigation were published in this work. It is a 4.7 μ m long asymmetric MZI modulator with a phase shift of 0.33π , an ER of 3dB, an IL of 2.9dB, and speed of 102GHz when operated at the bias voltage of 3.5V. The device length is carefully determined in consideration of the high transmission difference, the high ER, and the low IL of the system. When compared to the symmetric MZI modulator (41:59), the asymmetric MZI modulator (41:59) produces 0.4dB lower IL than the latter.

Increasing the oxide thickness of a device, while sacrificing modulation depth, may lower the device's capacitance and, as a result, enhance the RC-limited device bandwidth.

Additional to this, we present a design procedure for achieving customized metrics like modulation depth and speed as well as losses that allow engineers to construct modulators with specified functionality-based performance by extending the active material of choice to include more active materials. Despite the fact that there are new approaches to increasing the 3-dB bandwidth of semiconductor lasers to 100 GHz [33, 34], we can still boost the speed of ITO-based modulators beyond the intrinsic limit of ITO (300 GHz) by using advanced post fabrication techniques and improving the device's performance [35, 36].

Funding

This project is supported by AFOSR (#FA9550-21-1-0425) monitored by Dr. Gernot S. Pomrenke.

References

1. E. Heidari, et al. "Integrated ultra-high-performance graphene optical modulator." arXiv preprint arXiv:2109.07476 (2021).
2. C. Patil, et al. "1fJ/bit Coupling-based ITO Monolithic Modulator in Integrated Photonics." 2021 26th Microoptics Conference (MOC). IEEE, 2021.
3. H. Huang et al., "Chemical-sensitive graphene modulator with a memory effect for internet-of-things applications," *Microsystems and Nanoengineering*, vol. 2, no. September 2015, pp. 1–9, 2016, doi: 10.1038/micronano.2016.18.
4. T. Kondo, H. Watanabe, and T. Ohigashi, "Development of the Edge Computing Platform Based on Functional Modulation Architecture," *Proceedings - International Computer Software and Applications Conference*, vol. 2, pp. 284–285, 2017, doi: 10.1109/COMPSAC.2017.108.
5. W. Li, N. Zhang, Q. Liu, W. Feng, R. Ning, and S. Lin, "Scalable Modulation based Computation Offloading in Vehicular Edge Computing System," *IEEE Vehicular Technology Conference*, vol. 2020-Novem, pp. 20–24, 2020, doi: 10.1109/VTC2020-Fall49728.2020.9348752.
6. J. K. George et al., "Neuromorphic photonics with electro-absorption modulators," *Optics Express*, vol. 27, no. 4, p. 5181, 2019, doi: 10.1364/oe.27.005181.
7. R. Amin et al., "ITO-based electro-absorption modulator for photonic neural activation function," vol. 7, p. 81112, 2019, doi: 10.1063/1.5109039.
8. J. Park et al., "All-solid-state spatial light modulator with independent phase and amplitude control for three-dimensional LiDAR applications," *Nature Nanotechnology*, vol. 16, no. 1, pp. 69–76, 2021, doi: 10.1038/s41565-020-00787-y.
9. Q. Li, C. P. Ho, S. Takagi, and M. Takenaka, "Optical phase modulators based on reverse-biased III-v/si hybrid metal-oxide-semiconductor capacitors," *IEEE Photonics Technology Letters*, vol. 32, no. 6, pp. 345–348, 2020, doi: 10.1109/LPT.2020.2973174.
10. G. W. Lu et al., "High-temperature-resistant silicon-polymer hybrid modulator operating at up to 200 Gbit s⁻¹ for energy-efficient datacentres and harsh-environment applications," *Nature Communications*, vol. 11, no. 1, pp. 1–9, 2020, doi: 10.1038/s41467-020-18005-7.
11. M. Li, J. Ling, Y. He, U. A. Javid, S. Xue, and Q. Lin, "Lithium niobate photonic-crystal electro-optic modulator," *Nature Communications*, vol. 11, no. 1, pp. 1–8, 2020, doi: 10.1038/s41467-020-17950-7.
12. Z. Cheng et al., "Double-layer graphene on photonic crystal waveguide electro-absorption modulator with 12 GHz bandwidth," *Nanophotonics*, vol. 9, no. 8, pp. 2377–2385, 2020, doi: 10.1515/nanoph-2019-0381.
13. Z. Fan et al., "Characteristics of transition metal dichalcogenides in optical pumped modulator of terahertz wave," *AIP Advances*, vol. 10, no. 4, pp. 1–9, 2020, doi: 10.1063/1.5141511.
14. R. Amin et al., "Active material, optical mode and cavity impact on nanoscale electro-optic modulation performance," *Nanophotonics*, vol. 7, no. 2, pp. 455–472, 2017, doi: 10.1515/nanoph-2017-0072.
15. R. Amin et al., "Low-loss tunable 1D ITO-slot photonic crystal nanobeam cavity," *Journal of Optics (United Kingdom)*, vol. 20, no. 5, 2018, doi: 10.1088/2040-8986/aab8bf.

16. R. Amin et al., "Heterogeneously integrated ITO plasmonic Mach-Zehnder interferometric modulator on SOI," *Scientific Reports*, vol. 11, no. 1, pp. 1–12, 2021, doi: 10.1038/s41598-020-80381-3.
17. V. J. Sorger, N. D. Lanzillotti-Kimura, R. M. Ma, and X. Zhang, "Ultra-compact silicon nanophotonic modulator with broadband response," *Nanophotonics*, vol. 1, no. 1, pp. 17–22, 2012, doi: 10.1515/nanoph-2012-0009.
18. R. Amin, R. Maiti, J. B. Khurgin, and V. J. Sorger, "Performance Analysis of Integrated Electro-Optic Phase Modulators Based on Emerging Materials," *IEEE Journal of Selected Topics in Quantum Electronics*, vol. 27, no. 3, 2021, doi: 10.1109/JSTQE.2020.3041835.
19. R. Amin et al., "A Lateral MOS-Capacitor-Enabled ITO Mach-Zehnder Modulator for Beam Steering," *Journal of Lightwave Technology*, vol. 38, no. 2, pp. 282–290, 2020, doi: 10.1109/JLT.2019.2956719.
20. R. Amin et al., "0.52 μ m ITO-based Mach-Zehnder modulator in silicon photonics," *APL Photonics*, vol. 3, no. 12, pp. 0–11, 2018, doi: 10.1063/1.5052635.
21. R. Amin et al., "Sub-wavelength GHz-fast broadband ITO Mach-Zehnder modulator on silicon photonics," *Optica*, vol. 7, no. 4, p. 333, 2020, doi: 10.1364/optica.389437.
22. M. H. Tahersima et al., "Coupling-enhanced dual ITO layer electro-absorption modulator in silicon photonics," *Nanophotonics*, vol. 8, no. 9, pp. 1559–1566, 2019, doi: 10.1515/nanoph-2019-0153.
23. E. Li, Q. Gao, R. T. Chen, and A. X. Wang, "Ultracompact Silicon-Conductive Oxide Nanocavity Modulator with 0.02 Lambda-Cubic Active Volume," *Nano Letters*, vol. 18, no. 2, pp. 1075–1081, 2018, doi: 10.1021/acs.nanolett.7b04588.
24. M. A. Swillam, A. O. Zaki, K. Kirah, and L. A. Shahada, "On Chip Optical Modulator using Epsilon-Near-Zero Hybrid Plasmonic Platform," *Scientific Reports*, pp. 1–9, 2019, doi: 10.1038/s41598-019-42675-z.
25. N. C. Harris et al., "Quantum transport simulations in a programmable nanophotonic processor," *Nature Photonics*, vol. 11, no. 7, pp. 447–452, 2017, doi: 10.1038/nphoton.2017.95.
26. M. Dong et al., "High-speed programmable photonic circuits in a cryogenically compatible, visible-NIR 200 nm CMOS architecture," no. 21, 2021, [Online]. Available: <http://arxiv.org/abs/2105.12531>
27. C. Wang et al., "Integrated lithium niobate electro-optic modulators operating at CMOS-compatible voltages," *Nature*, vol. 562, no. 7725, pp. 101–104, 2018, doi: 10.1038/s41586-018-0551-y.
28. A. Liu, R. Jones, L. Liao, and D. Samara-rubio, "A high-speed silicon optical modulator based on a metal – oxide – semiconductor capacitor," vol. 427, no. February, pp. 615–618, 2004, doi: 10.1038/nature02279.1.
29. S. Koeber et al., "Femtojoule electro-optic modulation using a silicon-organic hybrid device," *Light: Science and Applications*, vol. 4, no. 2, 2015, doi: 10.1038/lsa.2015.28.
30. Z. Ma, Z. Li, K. Liu, C. Ye, and V. J. Sorger, "Indium-Tin-Oxide for High-performance Electro-optic Modulation," *Nanophotonics*, vol. 4, no. 1, pp. 198–213, 2015, doi: 10.1515/nanoph-2015-0006.
31. Y. Gui et al., "Towards integrated metatronics: a holistic approach on precise optical and electrical properties of Indium Tin Oxide," *Scientific Reports*, vol. 9, no. 1, pp. 1–10, 2019, doi: 10.1038/s41598-019-47631-5.
32. H. Dalir, et al. Atto-Joule, high-speed, low-loss plasmonic modulator based on adiabatic coupled waveguides. *Nanophotonics*7(5), 859–864 (2018).
33. E. Heidari, et al. "VCSEL with multi-transverse cavities with bandwidth beyond 100 GHz." *Nanophotonics* 10.14 (2021): 3779-3788.
34. E. Heidari, et al. "Hexagonal transverse-coupled-cavity VCSEL redefining the high-speed lasers." *Nanophotonics* 9.16 (2020): 4743-4748.
35. A., Moustafa, et al. "Structural, electrical, and optical properties of ITO thin films and their influence on performance of CdS/CdTe thin-film solar cells." *Journal of Materials Science: Materials in Electronics* 32.8 (2021): 11107-11118.
36. A. Moustafa, et al. "The main role of thermal annealing in controlling the structural and optical properties of ITO thin film layer." *Optical Materials* 113 (2021): 110866.

Supplementary Information

Yaliang Gui¹, Mario Miscuglio¹, Rubab Amin¹, Hao Wang¹, Jacob K. Khurgin, Hamed Dalir^{1,a}, and Volker J. Sorger¹

100 GHz Micrometer-compact broadband Monolithic ITO Mach–Zehnder Interferometer Modulator enabling 5000 times higher Packing Density

¹Department of Electrical and Computer Engineering, George Washington University, Washington, DC 20052, USA

²Department of Electrical and Computer Engineering, Johns Hopkins University, Baltimore, Maryland 21218, USA

a) Author to whom correspondence should be addressed: hdalir@gwu.edu

i. Analysis of arbitrary power splitter-based Mach Zehnder Modulator performance (Plasmonic mode)

An asymmetric power splitter based MZI is consist of Y-junction with specific splitting ratio on the input side and a Y junction with splitting ratio of 50:50 on the output side. A plasmonic mode ITO modulator is place on the active arm to shift the phase. Here we use plasmonic mode ITO modulator as an example because of merits such as small footprint, potential of high speed and high modulation depth. However, high modulation depth is accompanied with high propagating loss which is indicated by Kramers–Kronig relations. The influence of propagating loss is also discussed in this paper.

For π shift device, high ER can be achieved by compensating device propagating loss with higher splitting power (splitting ratio > 50) or using balance device on the passive arm. Low IL can be achieved at the same time by changing the device length or by using different MZI arm lengths. By using asymmetric arms, the initial phase difference, $\Delta\varphi_{initial}$, caused by different effective mode index of two arms can be precisely controlled (fig a,b,8c). Depending on the input signal, the initial phase difference, $\Delta\varphi_{initial}$, is the same with the OFF state (0V) phase difference for applications that use either positive or negative bias, while for applications that use both positive and negative bias, OFF state phase difference under negative bias would be discussed instead of the initial phase difference. Since phase difference shift forward under negative bias and vice versa. The transmission, ER and IL can be calculated by using:

$$T = \frac{(\frac{\sqrt{x}}{10} E_{in} e^{-\frac{\alpha}{2}L})^2 + (\frac{\sqrt{100-x}}{10} E_{in})^2}{2} + \frac{2 \times (\frac{\sqrt{x}}{10} E_{in} e^{-\frac{\alpha}{2}L}) \times (\frac{\sqrt{100-x}}{10} E_{in}) \times \cos(\Delta\varphi_{initial} + \Delta\varphi_{bias})}{2} \quad (1)$$

$$ER = 10 \cdot \lg\left(\frac{T_{max}}{T_{min}}\right) \quad (2)$$

$$IL = 10 \cdot \lg(T_{max}) + L_{facet} \times 2 \quad (3)$$

$$\Delta\varphi_{bias} = \pi \text{ (For } \pi \text{ phase shift device)} \quad (4)$$

(E_{in} , x , α , L , $\Delta\varphi_{initial}$, $\Delta\varphi_{bias}$ and L_{facet} are the input electric field phasor, the splitting ratio on the active arm side, device absorption coefficient, device length, the initial phase difference caused by different effective mode index between device and waveguide, phase changed by bias and facet coupling loss). Here we assume there is a π phase shift ITO plasmonic device with effective mode index of 2.5, $\alpha \cdot L = 0.2$ under 0 V and $\alpha \cdot L = 0.26$ under V_{π} . (fig. 1e and 1f) The initial phase difference is eliminated by using different MZI arms or using balanced device. L_{facet} is 0.07dB obtained from Lumerical simulation. Power with high splitting ratio ($x=60$) on the active arm compensate the propagating loss and is used in application requires high ER. Low splitting ratio power ($x=37$) in contrast decrease the insertion loss by reducing the modulation depth. The overall transmissions decrease with increasing power splitter ratio because of the increasing propagating losses. Symmetric MZI with balance device has as high ER as asymmetric MZI modulator (60:40) but has 8% weaker transmission. Device with free choice of power splitting ratio is preferred than the device with balance device considering the IL.

For small phase shift device, high ER and low IL cannot be obtained at the same time. The free choice of splitting ratio provides more options for different application. High splitting ratio for applications that requires high ER, while low splitting ratio for applications with high IL requirements. What's more, the $\Delta\varphi_{initial}$ should be carefully chosen for different applications.

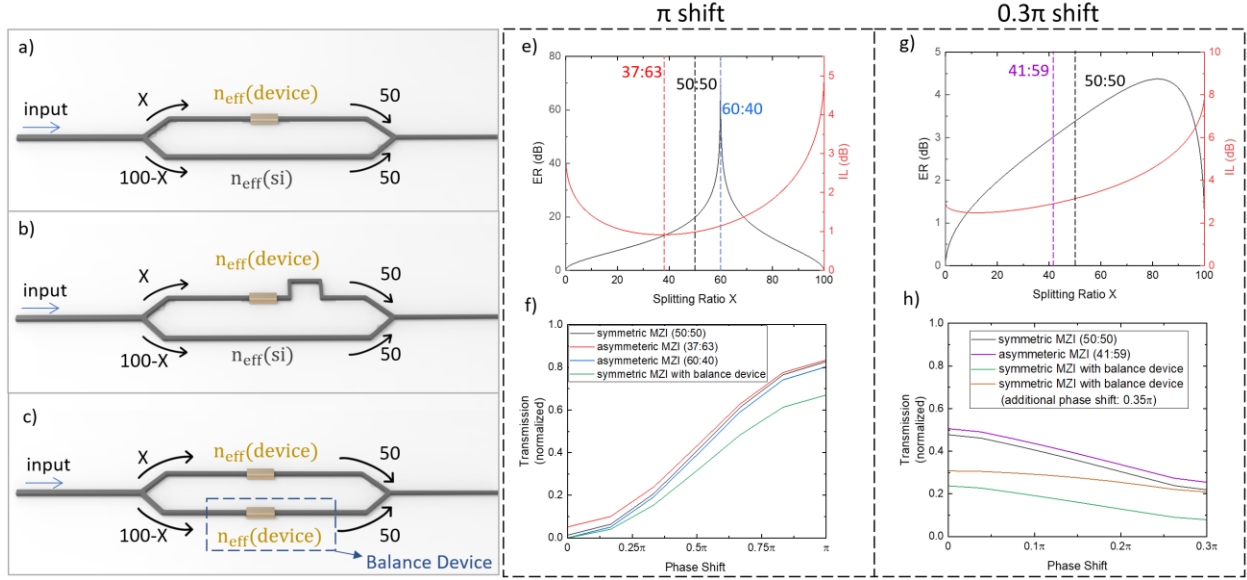


Figure 1 Performance analysis for MZI modulator with free choice power splitting ratio. a) MZI modulator with arms of the same length. b) MZI with different arm length which is used to tune the OFF-state phase shift to $k\pi$, $k=0,1,2,\dots$ c) MZI modulator with balance device on passive arm. The initial phase shift is 0. e) ER and IL of π phase shift device under different splitting ratio. (Device with power splitting ratio of 37:63 has lowest IL of 0.9dB and ER of 13dB; device with power splitting ratio of 50:50 has IL of 1dB and ER of 20dB, and device with power splitting ratio of 60:40 has IL of 1.1dB and ER of 70dB.) f) Normalized transmission of different splitting ratio (50:50, 37:63 and 60:40) and with balance device under bias with π phase shift. IL and ER of symmetric MZI modulator with balance device is 1.7dB and >70dB respectively. g) ER and IL of 0.3π phase shift device under different splitting ratio. h) Normalized transmission of different splitting ratio (50:50, 37:63 and 60:40) and with balance device under bias with 0.33π phase shift.

Here, plasmonic mode ITO-based MZI modulator 0.33π phase shift is used as an example of small phase shift device. The performances including the ER and IL is lower than previous π shift design because of weak modulation depth. However, it's useful for most of applications. The performance of symmetric MZI modulator with balance device can be optimized according to the application by using additional phase shift. Still comparing with the asymmetric MZI modulator, it's not a good choice.

ii. Arbitrary power splitter-based photonic mode ITO MZI modulator

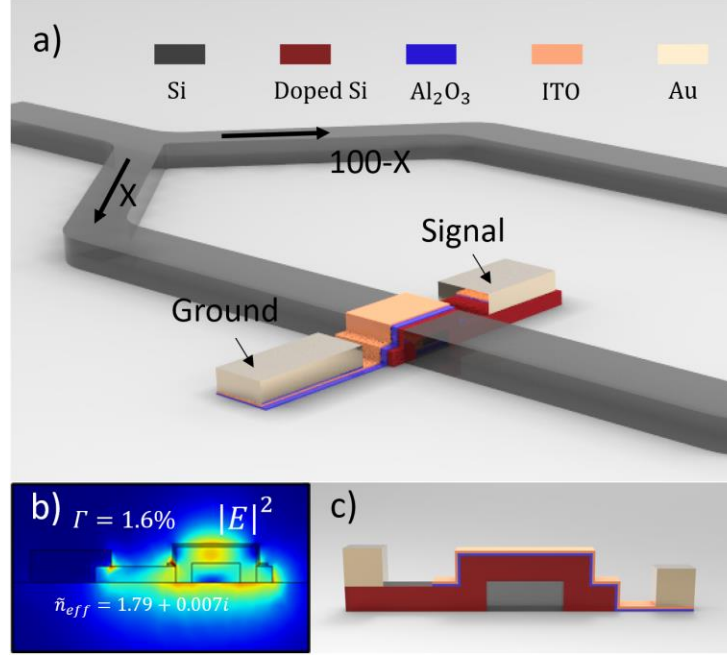


Figure 2 ITO-based Photonic mode MZI modulator on Si photonic platform. (a) Perspective view of the Mach-Zehnder structure with the active biasing contacts. The power splitting ratio for the active arm is X, and the splitting ratio for the passive arm is 100-X. (b) Electric field distribution by performing FEM at 1550nm under +3.5V in the cross-sectional structure for a z cutline along the central region of the Si waveguide (width: 500nm; height: 220nm). (c) Composition layers of ITO MZI modulator. ($T_{doped\ silicon} = 100nm$; $T_{Al_2O_3} = 10nm$; $T_{ITO} = 10nm$; $T_{Au} = 50nm$)

Photonic mode ITO based modulator design: The photonic mode ITO-based modulator design with an asymmetrical MZI is based on a silicon-on-insulator (SOI) platform. A Y-junction has been carefully designed as a power splitter with an arbitrary (non 50:50) splitting ratio as a function of device loss on the input side and a 50:50 Y-junction on the output side to balance the power of each arm. For photonic mode device option, the silicon is highly doped at the device area as the bottom contact with a doping concentration of $10^{20} cm^{-3}$ giving a conductivity of 97087 S/m. The doping depth must be not too thin as to ensure a low resistance and was selected here to be 100nm. The complex refractive index[3] of doped silicon at 1550nm is calculated as:

$$n_{doped} = n_{intrinsic} + \Delta n$$

$$k_{doped} = k_{intrinsic} + \Delta k$$

$$\Delta\alpha = (4 \cdot \Delta k \cdot \pi) / \lambda$$

$$\Delta\alpha = \Delta\alpha_e + \Delta\alpha_h = 8.88 \times 10^{-21} \times \Delta N_e^{1.167} + 5.84 \times 10^{-20} \times \Delta N_h^{1.109}$$

$$-\Delta n = \Delta n_e + \Delta n_h = 5.4 \times 10^{-22} \times \Delta N_e^{1.011} + 1.53 \times 10^{-18} \times \Delta N_h^{0.838}$$

Where, $\Delta\alpha_e$, $\Delta\alpha_h$, Δn_e , Δn_h , are absorption coefficient change by doped electrons and holes, respectively, and the refractive index change again arising from doped electrons and holes, number of electrons introduced through doping, respectively. ΔN_e and ΔN_h are the carrier concentrations for both charges introduced by doping. $n_{intrinsic} = 3.48$ and $k_{intrinsic} = 0$. The carrier concentration of unbiased ITO thin film is $2.07 \times 10^{20} cm^{-3}$. Under $\pm 5V$, the refractive

indexes for 10nm ITO thin film are $1.7896+0.007686i$ and $1.6539+0.00261i$. a 10nm thin Al_2O_3 film between ITO thin film and doped silicon region is used as gating oxide. The anticipated speed is 108GHz.

Photonic mode ($\pm 5V$)

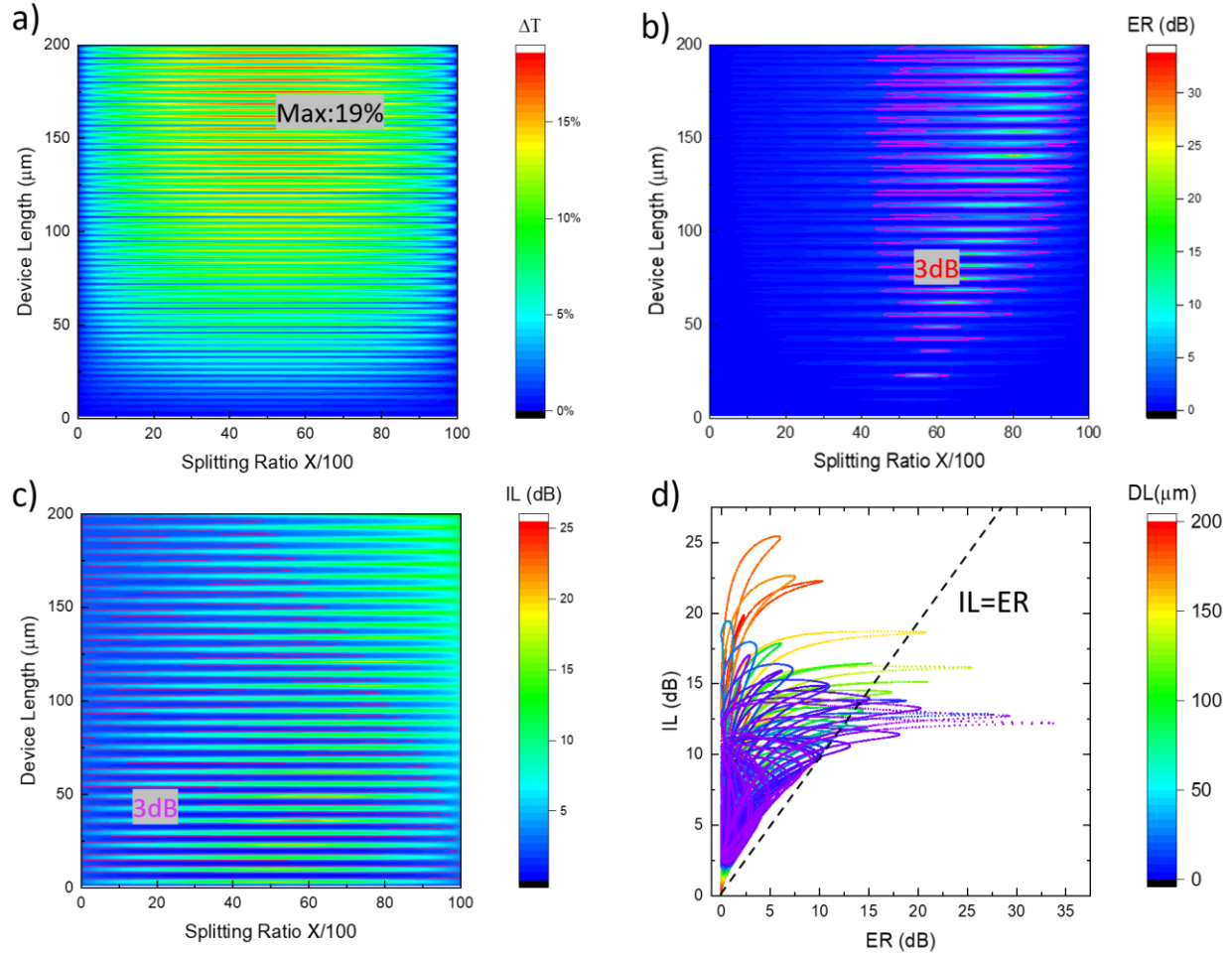


Figure 3 The performance map of asymmetric photonic mode ITO-based MZI modulator with 15nm Al_2O_3 under ON (-5V) and OFF states (+3.5V). a) Transmission difference varies with splitting ratio X and device length $0 \mu m$ to the maximum transmission difference of the photonic mode device is 19% because of weak modulation depth. Photonic mode designs with high transmission differences locate in long-length regions because of weak modulation depth and low device loss. b) Extinction ratio of photonic device varies with splitting ratio for different lengths. c) Insertion loss of plasmonic mode and photonic mode varies with splitting ratio for different lengths. d) Performance map for device length ranging length from $0.1 \mu m$ to $20 \mu m$.

References:

- [1] Z. Ma, Z. Li, K. Liu, C. Ye, and V. J. Sorger, “Indium-Tin-Oxide for High-performance Electro-optic Modulation,” *Nanophotonics*, vol. 4, no. 1, pp. 198–213, 2015, doi: 10.1515/nanoph-2015-0006.
- [2] J. Meng, M. Miscuglio, J. K. George, A. Babakhani, and V. J. Sorger, “Electronic Bottleneck Suppression in Next-Generation Networks with Integrated Photonic Digital-to-Analog Converters,” *Advanced Photonics Research*, vol. 2, no. 2, p. 2000033, 2021, doi: 10.1002/adpr.202000033.
- [3] M. Nedeljkovic, R. Soref, and G. Z. Mashanovich, “Free-carrier electrorefraction and electroabsorption modulation predictions for silicon over the 1-14- μm infrared wavelength range,” *IEEE Photonics Journal*, vol. 3, no. 6, pp. 1171–1180, 2011, doi: 10.1109/JPHOT.2011.2171930.